Supporting Information

Molecular and Coarse-Grained Modelling to Characterize and Optimize Dendrimer-Based Nanocarriers for siRNA Delivery

Filip Stojceski[1], Gianvito Grasso[1,*], Lorenzo Pallante[2], and Andrea Danani[1,*]

[1] Istituto Dalle Molle di studi sull'Intelligenza Artificiale (IDSIA), Scuola universitaria professionale della Svizzera italiana (SUPSI), Università della Svizzera italiana (USI), Centro Galleria 2, Manno, CH-6928, Switzerland.

[2] PolitoBIOMed Lab, Department of Mechanical and Aerospace Engineering. Politecnico di Torino

[*] Corresponding Author

S.1 All-Atom Molecular Dynamics of DM and DP

DM and DP three dimensional systems has been generated using Avogadro chemical editor[1]. The R.E.D. Tools[2] was adopted to define partial charges, adopting GAMESS-US[3] as geometry optimization and molecular electrostatic potential (MEP) computation program. The Hartree–Fock (HF) method at the 6-31G* basis set was used to optimize molecular geometries. Two stage RESP fitting was performed in order to obtain dendrimers MEP-derived partial charges, after MEP computation at HF/6-31G* theory level. The General Amber Force Field (GAFF)[4] has been chosen to describe dendrimers topologies. Therefore, each dendrimer was set in the center of dodecahedron box, solvated with water and filled with ions (Cl- and Na+) at concentration of 0.15M. GROMACS 2018.3[5,6] package was adopted for performing MD simulations. Position restrain MD of 100 ps in respectively NVT ensemble using v-rescale[7] thermostat at 300K and NPT ensemble using Berendsen[8] barostat at 1 atm was carried out, after a process of 1000 steps of steepest descent energy minimization. Production MD simulation of 100 ns in NPT ensemble using Parinello-Rahman[9] barostat was performed on both dendrimers. Long-ranged electrostatic interactions were calculated at every step with the Particle-Mesh Ewald (PME)[10] method with a cut-off of 1 nm. A cut-off of 1 nm was also applied to Lennard-Jones[11] interactions. Last 20 ns of production trajectory was extracted considering that simulation has reached equilibrium, on which the starting topological parameters of the CG model was calculated. Radius of Gyration (RG) and Solvent Accessible Surface Area (SASA) were taken in account to evaluate if DM and DP systems has been reached the equilibrium (*Figure S1*).
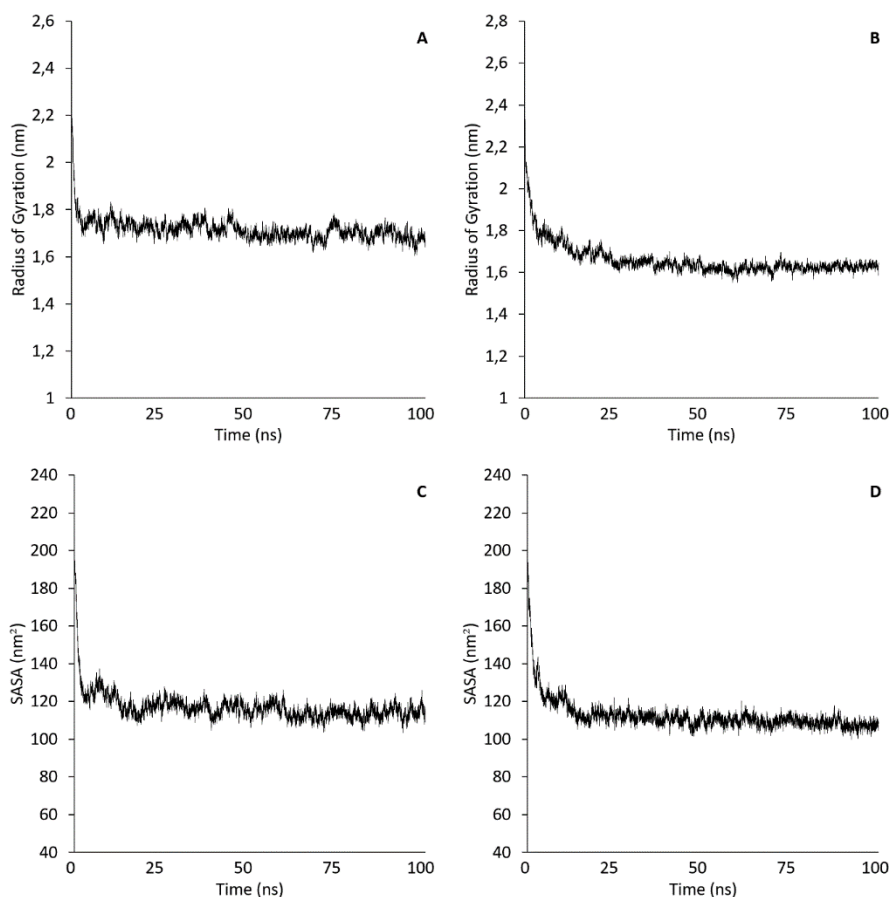
Figure S1: Radius of Gyration (RG) of DM and DP over 100 ns of all atomistic production simulation are showed respectively in figure A and B, while in figure C and D the Solvent Accessible Surface Area (SASA) of DM and DP over 100ns of all atom production simulation are showed respectively.

S.2 Features of CG Maps

The Coarse Grained (CG) molecule maps have been developed following the CG Martini [12] strategy, which implies to group atomistic particles in CG beads each composed by 2-3 or 4-5 heavy atoms. These maps have been designed to allow conformational changes and rotations (*Figure S2*) of specific atoms zones in dendrimers CG models, seen in Molecular dynamics (MD) atomistic simulations:

- Flipping between methyl and thiophosphoric groups, around the nitrogen atoms, which allows translation of the next connected branches.
- Torsion of the bond between nitrogen and phosphorus atoms that allows rotations of the next connected branches.

These two characteristics, in addition to controlled movements of branches that starts from cyclo-phosphazene ring, are fundamental to mimic the dendrimers mobility showed in atomistic MD to the CG models.
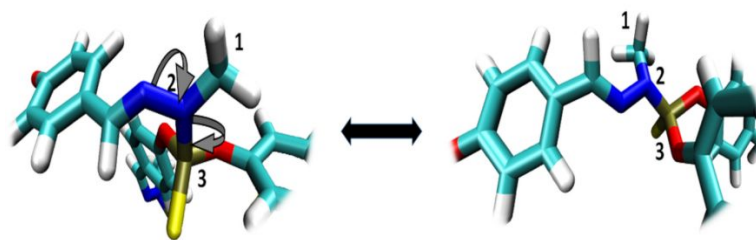
Figure S2: Representation of flipping between methyl (1) and thiophosphoric (3) group, around the nitrogen (2) atom, and torsion of the bond between nitrogen (2) and phosphorus atom (3).

Indication of CG particles employed to define CG beads are shown in Table S1, where Beads, Smiles code of the mapped atomistic groups and Particle type are reported. Mapping employed only existent CG particles [12].

Table S1: Description of the dendrimer beads used for CG Mapping. Beads, Smiles code of the mapped atomistic groups and particle type are reported.

Bead	Smiles (Atomistic Structure)	Type
SP_1	NP=N	POLAR
SN_0	OC(=C)C	NON POLAR
SC_4	C =CC	APOLAR
SC_2	CC	APOLAR
N_0	N(C)NP	NON POLAR
SP_2	P=S	POLAR
Q_0	NCC[N+]	CHARGED (+1)
N_0	CCOCC	NON POLAR
C_1	CCCC	APOLAR

More in detail:

✓ SP_1 bead has been chosen to describe the atomic group [NP=N]; the presence of the phosphorous and the nitrogen atoms may justify the choice of slightly polar bead. Low polar bead has been chosen also for avoid too high affinity with the water ones, which could give anomalous movements to the central ring.

- ✓ **SN₀** bead (4 CG particles [OC(=C)C]) maps oxygen atom and orto benzene atoms. The chosen SN_0 particles are smaller than regular N_0 beads[12]. All particles are connected by constraints to preserve rigidity of the structure and avoid fast oscillation of the ring.

- ✓ **SC₄** bead (3 CG particles [C=CC]) maps meta and para benzene atoms[12,13]. All particles are connected by constraints to preserve rigidity of the structure and avoid fast oscillation of the ring.

- ✓ **SC₂** bead represents the atomic group [(C=N)NC]. The group is considered non-polar. Reasons lies in double bonds made by nitrogen atoms. Those double bonds make the establishment of hydrogen bonds unlikely. Moreover, the non-polar characteristics is also justified by the shield effect of the methyl group.

- ✓ **N₀** bead maps the atomic group [N(C)NP]. The group is considered non-polar. Reasons lies in double bonds made by nitrogen atoms. Those double bonds make the establishment of hydrogen bonds unlikely. Moreover, the non-polar characteristics is also justified by the shield effect of the methyl group. Phosphorous atoms are used only for center the bead around the planar chiral nitrogen.

- ✓ **SP₂** bead maps the atomic group [P=S] as previously done in literature [12].

- ✓ **Q₀** bead maps the atomic group [NCC[N+]]. The CG particle is positively charged (+1). The choice is in agreement with the coordinated covalent bond between nitrogen and hydrogen. Similar chemical groups have been mapped with Q_0 in DPPC phospholipids in literature [12].

- ✓ **N₀** (Terminal) bead maps the atomic group [CCOCC]. Five atoms single bead was chosen to maintain the symmetry of the cyclic structure in comparison to the pyrrolidinium terminal, just increasing polarity to N type bead for the presence of oxygen atom.

- ✓ **C₁** (Terminal) bead maps the atomic group [CCCC] as previously done in literature [12].

S.3 Modified Boltzmann Inversion

CG simulation method[14] has been proven in recently years as efficient and reliable commonly used technique to explore biological systems for greater length and time scales in comparison with atomistic method. To allow the switching from atomistic to CG models significant efforts must be performed in generating the correct bond parameters in order to emulate also the atomistic mechanical proprieties. Topological parameters adopted in CG simulations are often derived using one of the cited technics in previously chapter, like for example iterative Boltzmann inversion[15–17] (IBI). IBI methodology is based on the Boltzmann inversion[18,19] equation:

$$V(r) = -k_B T \ln(g(r)) \tag{1.1}$$

Where $V(r)$ is the potential energy, k_B is the constant of Boltzmann, T is absolute temperature and g (r) is the distribution function between a pair of sites. Afterwards, iteration process begins, leading in a correction of starting potential:

$$V_{i+1}(r) = V_i - \alpha k_B T \frac{\ln(g(r)_i)}{\ln(g(r)_{i+1})} \qquad (1.2)$$

Where V_{i+1} is the actual potential energy, V_i is the previous potential energy, k_B is the constant of Boltzmann, T is absolute temperature, $g(r)_{i+1}$ is the distribution function and α is called dumping factor which prevents abnormal variation of the potential energy, during the iteration procedure. Extracting the distribution function $g(r)$ from equation (1.1) we can obtain the following equivalence:

$$e^{-V(r)/k_B T} = e^{-K(x-\mu)^2/2k_B T} \qquad (1.3)$$

$$e^{-(x-\mu)^2/2\sigma^2} \leftrightarrow e^{-K(x-\mu)^2/2k_B T} \qquad (1.4)$$

Where $\frac{K(x-\mu)}{2}$ is a generic harmonic potential $V(r)$. Equivalence 1.4 is valid only if it is true that the standardized normal distribution (Gauss distribution) can be considered equivalent to the target functional form, since taking the assumption of independent degrees of freedom, and hence no correlation. Finally, simply replacing new assumed $g(r)$ in the equation 1.1, it results:

$$V(r) = -k_B T \ln(g(r)) = -k_B T \ln\left(e^{-(x-\mu)^2/2\sigma^2}\right) = -k_B T \frac{-(x-\mu)^2}{2\sigma^2} \qquad (1.5)$$

$$V(r) = -\frac{K(x-\mu)^2}{2} = -k_B T \frac{-(x-\mu)^2}{2\sigma^2} = \frac{k_B T}{\sigma^2} \qquad (1.6)$$

Such particular computing method of Boltzmann inversion[18,19] technique is applicable for the estimation of the bonds, angles and constraint topological parameters, only using standard deviation σ to get harmonic constant K. As for IBI computation, even equation 1.6 can be used to implement an iterative modified Boltzmann inversion:

$$V_{i+1}(r) = V_i(r) \pm \beta V_i(r) \frac{\sigma^2_{i+1}}{\sigma^2_i} \qquad (1.7)$$

Where β is a value with the aim of modulating abrupt variation of potential energy values, like IBI-dumping constant, whose range is from 0 to 1. In conclusion, the correction factor $+\beta V_i(r) \frac{\sigma^2_{i+1}}{\sigma^2_i}$ is adopted if σ^2_{i+1} is greater than σ^2_i, contrariwise $-\beta V_i(r) \frac{\sigma^2_{i+1}}{\sigma^2_i}$ is selected if σ^2_{i+1} is lower than σ^2_i.

S.4 Topological Parameter Validation

Topological bonded parameters has been tuned up with the goal to achieve convergence on all the bond terms distribution[20–22]. Then, ratio of the averages and standard deviation (SDEV) between atomistic and CG angles distributions $\left(\frac{meanATOMISITC}{meanCG}; \frac{sdevATOMISITC}{sdevCG}\right)$ over the time are shown in Figure S3. We consider acceptable value in the range from 0,7 to 1,3 to validate bond terms.
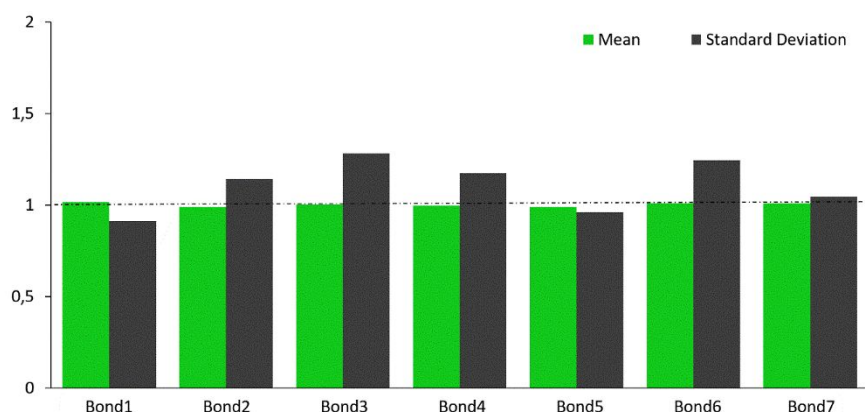

Figure S3: Bar diagram which evidence the comparison of bond parameters, in light-green is show mean of each bonds ratio, in dark green is show standard deviation of each bonds ratio. Ratio between value 0,7 and 1,3 are considered satisfactory for validation. Ratio are computed making the quotient between the atomistic mean or standard deviation and CG mean or standard deviation.

Notably, *Figure S3* shows a perfect matching values for means of each bonds, while SDEV tends to be greater than 1.0, because CG Martini[12] models need higher potential energy to maintain the same mean in comparison with atomistic mean. This behavior leads into generation of slightly stiffer CG model. Therefore, some bonds have not been taken into consideration because they were set as constraints. These bonds were assumed as constraints when the force constant (K_b) was greater than 10^6 KJ mol^{-1} nm^{-2}. Indication of each number of bonds illustrated in *Figure S3* is show in *Table S2*, where bonds number and bonds type are reported.

Table S2: Description of the bond parameters with bond number and bond type.

Bond number	Bond type
Bond 1	SP_2 - Q_0
Bond 2	Q_0 - N_0
Bond 3	SP_2 - SN_0
Bond 4	SC_2 - N_0
Bond 5	N_0 - SP_2
Bond 6	SP_1 - SN_0
Bond 7	Q_0 - C_1

Next topological terms tuned up are the angles parameters, following the same procedure adopted before. Then, ratio of the averages and SDEV between atomistic and CG angles distributions $\left(\frac{meanATOMISITC}{meanCG}; \frac{sdevATOMISITC}{sdevCG}\right)$ over the time are shown in *Figure S4*. Even in this case, value in the range from 0,7 to 1,3 are considered acceptable. Again, we can clearly observe that keeping the average in the desired range is easier than keeping the SDEV in the right zone. As we can see in both *Figure S3* and *Figure S4* the values of SDEV has the tendency to be higher than 1.0, which means that the SDEV of the atomistic bonded parameters is higher than that of the CG bonded parameters. This is in agreement with the general characteristics of the Martini force field[12,23] which has a greater rigidity on bonded parameters in comparison to atomistic models, due to the reduction of the degrees of freedom. Indication of each number of considered angles is shown in *Table S3*, where angles number and angles type are reported.
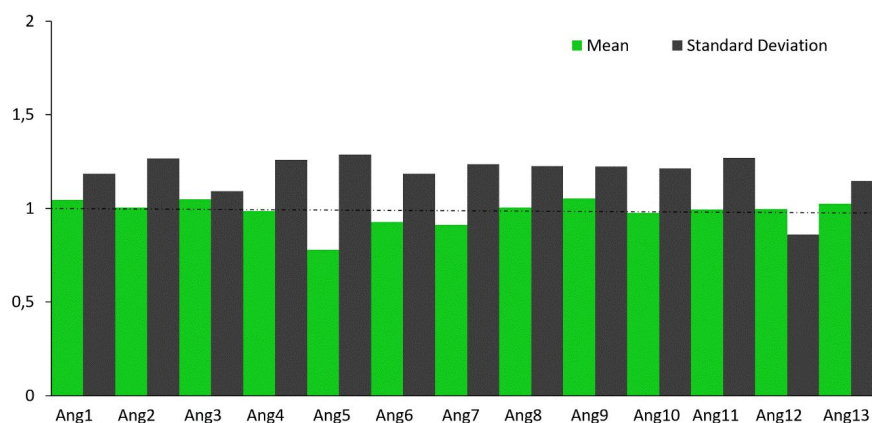

Figure S4: Bar diagram which evidence the comparison of angle parameters, in light-green is show mean of each angles ratio, in dark green is show standard deviation of each angles ratio. Ratio between value 0,7 and 1,3 are considered satisfactory for validation. Ratio are computed making the quotient between the atomistic mean or standard deviation and CG mean or standard deviation.

Table S3: Description of the angle parameters with angle number and angle type.

Angle number	Angle type
Ang 1	Q_0 - SP_2 - Q_0
Ang 2	SC_2 - N_0 - SP_2
Ang 3	SP_2 - Q_0 - N_0
Ang 4	SN_0 - SP_2 - SN_0
Ang 5	N_0 - SP_2 - SN_0
Ang 6	N_0 - SP_2 - Q_0
Ang 7	SC_4 - SC_2 - N_0
Ang 8	SP_2 - SN_0 - SC_4
Ang 9	SN_0 - SP_1 - SN_0
Ang 10	SP_1 - SP_1 - SN_0
Ang 11	SP_1 - SN_0 - SC_4
Ang 12	SN_0 - SC_4 - SC_2
Ang 13	SP_2 - Q_0 - C_1

Since mean and SDEV were used to validate bond and angle parameters assuming that the distributions are Gaussian, some examples of distribution are shown in Figure S5. The extreme attention in the choice of the GC maps was done to have Gaussian-like distributions that can be easily reproduced with the Martini[12] system. In addition, it must be remembered that the iterative process of tuning the bonds and angles was done assuming that the distributions are Gaussian-like.
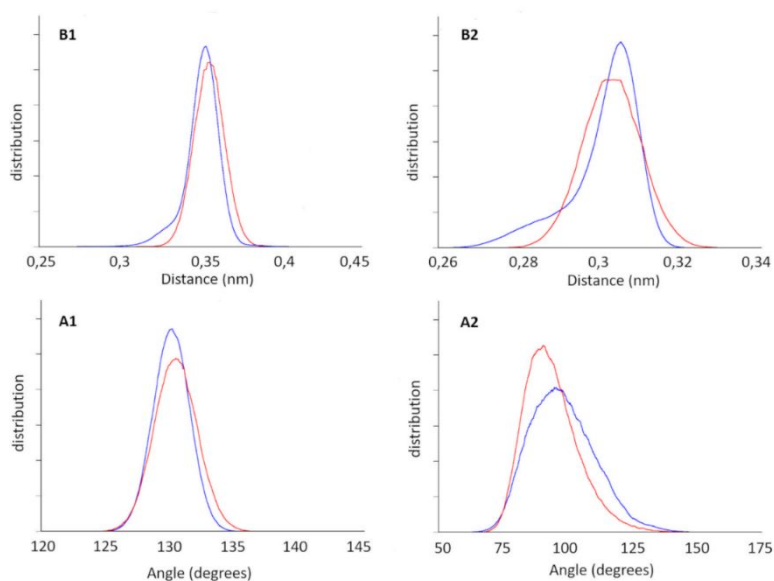

Figure S5: Example of distributions of four bonded parameters: B1 and B2 are distributions of two bonds terms, instead A1 and A2 are distributions of two angles terms. In blue atomistic distributions are shown, while in red the CG ones are represented.

Furthermore, to keep the vibrations of the chains respect to the central core in the same range as in the atomistic model, 3 Ryckaert-Bellemans potential[24] has been introduced for the dihedral angles between the core and the 6 chains (*Figure S6*). The beads involved into before mentioned dihedral potential are shown in the
Table S4.

Table S4: Description of the dihedrals parameters with dihedral number and dihedral type.

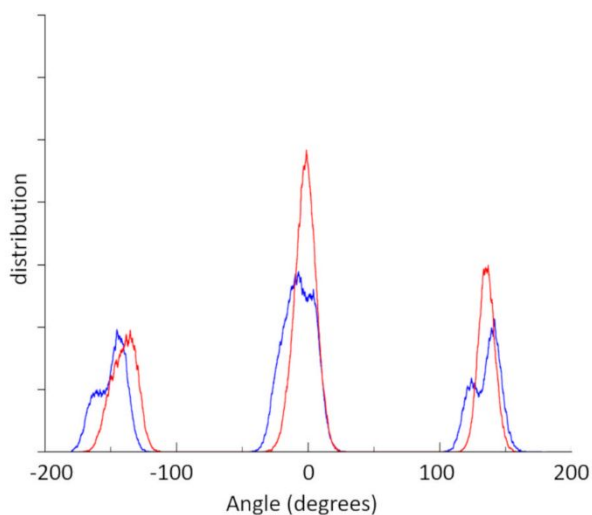| Dihedral angle	Dihedral type
Dih 1	SN_0 - SP_1 - SP_1 - SN_0

Figure S6: Ryckaert-Bellemans dihedral potential applied between core and the 6 chains. In blue is represented the atomistic distribution, while in red is shown the CG distribution. The imposed CG dihedral well emulates the reference atomistic dihedral.

Conformational Analysis

After the modulation of bonded terms, we continue the validation exploring the conformational characteristics. Structural conformation of both CG dendrimer models was evaluated in comparison with atomistic models by measuring mean and standard deviation of the radius of gyration (RG) and root mean square fluctuation (RMSF). As shown in *Figure S7*, averages of the CG RGs are very close to the reference atomistic RGs, and the SDEV seems to have the same behavior.
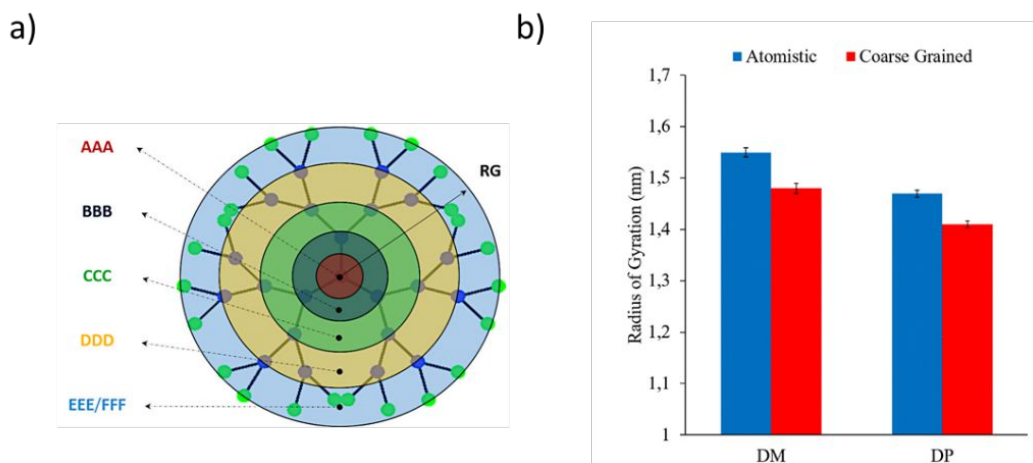
Figure S7: a) Representation of the spherical-shell-like division (sub-units) used to perform RG and RMSF analysis. b) Radius of gyration (RG) of morpholinium dendrimer (DM) and pyrrolidinium dendrimer (DP): comparison between atomistic model (blue) and coarse grained model (red).

In *Figure S8* the mean and SDEV of RMSF are shown divided by sub-units of the atomistic dendrimers chain structure (blue*)*, which are also quite good maintained in CG models (red). Fluctuation of the chain terminals (please see *Figure S7a)* is very important for the binding capacity of the dendrimers. If CG terminals results too much stiff respect to the atomistic ones, probably they will be no more able to properly bind target molecule. Since all before mentioned analysis demonstrated a good correlation between atomistic and CG DM and DP, we are going to use these models to perform CG MD simulations in order to shed light on stoichiometric and competition phenomes.
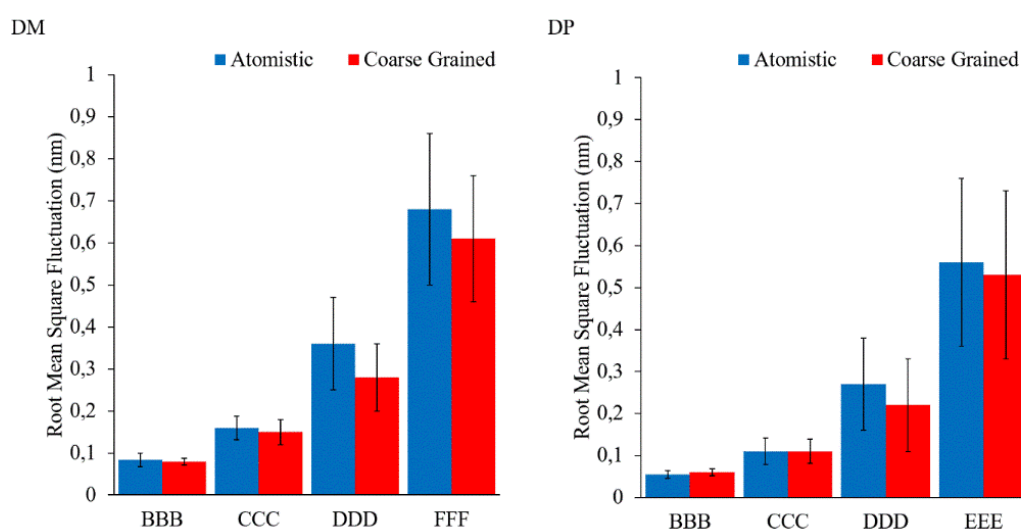

Figure S8: Root mean square fluctuation (RMSF) of morpholinium dendrimer (DM) and pyrrolidinium dendrimer (DP) calculated and divided by residues, represented through mean with standard deviation. In blue atomistic RMSF values are plotted, in red CG ones.

S.5 siRNA Bending Angle

With the aim to quantitative measure the siRNA structural bending, we have adopted the bending angle parameter "θ", as shown in *Figure S9*, which is the angle between two vectors, formed by connecting the siRNA's center with the two extremities. The siRNA center and the extremes have been considered as points identified by their COMs (*Figure S9*). As a result, DP has induced only a slight conformational change in the siRNA structure, by flexing the filament with bending angle in average equal to 151° (*Figure S9*). This result is in line with the bending of a siRNA molecule alone in water environment (158°). Instead, DM significantly wraps the siRNA's structure by bending till an average value around 137° (*Figure S9*).
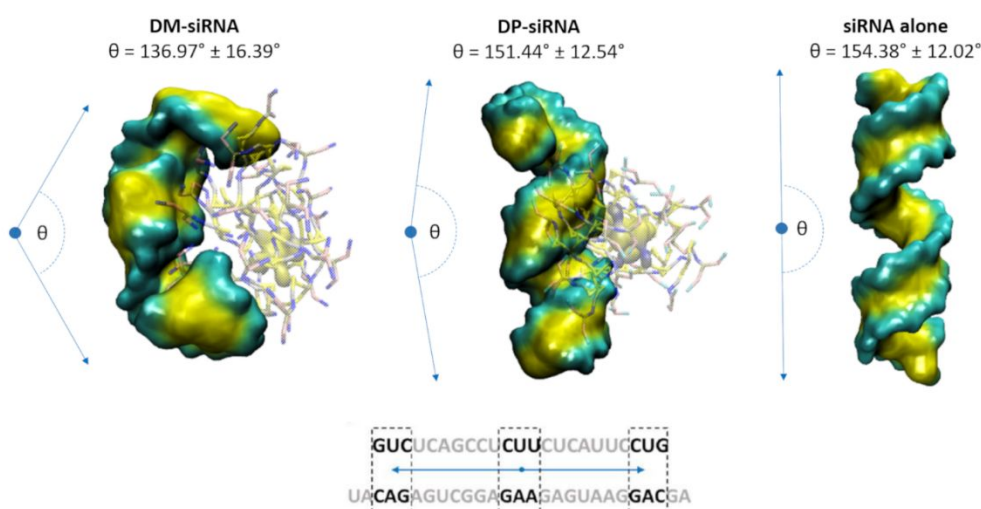

Figure S9: Conformational analysis of siRNA computed using parameter θ, which quantify the flexion caused by dendrimer. An indication of chosen point for calculating angle θ, estimated as center of mass (COM) of nucleotide triplets, are also reported. In this picture it is shown how values of angle θ can change considering 3 main cases: DM-siRNA, DP-siRNA and siRNA alone.

S.6 Dendrimer competition phenomena

Figure S10 shows a qualitative representation of the interaction between dendrimers and siRNA double filaments. In *Figure S10*A-C only the complexed dendrimer with siRNA are showed, while in *Figure S10*B-D both dendrimers complexed with siRNA are represented. In detail, picture A shows 1 DM in complexation with siRNA (27% of MD frames), while picture B displays 2 DM in complexation with siRNA (73% of MD frames). Picture C shows 1 DP in complexation with siRNA (53% of MD frames), while picture D represents 2 DP in complexation with siRNA (47% of MD frames).
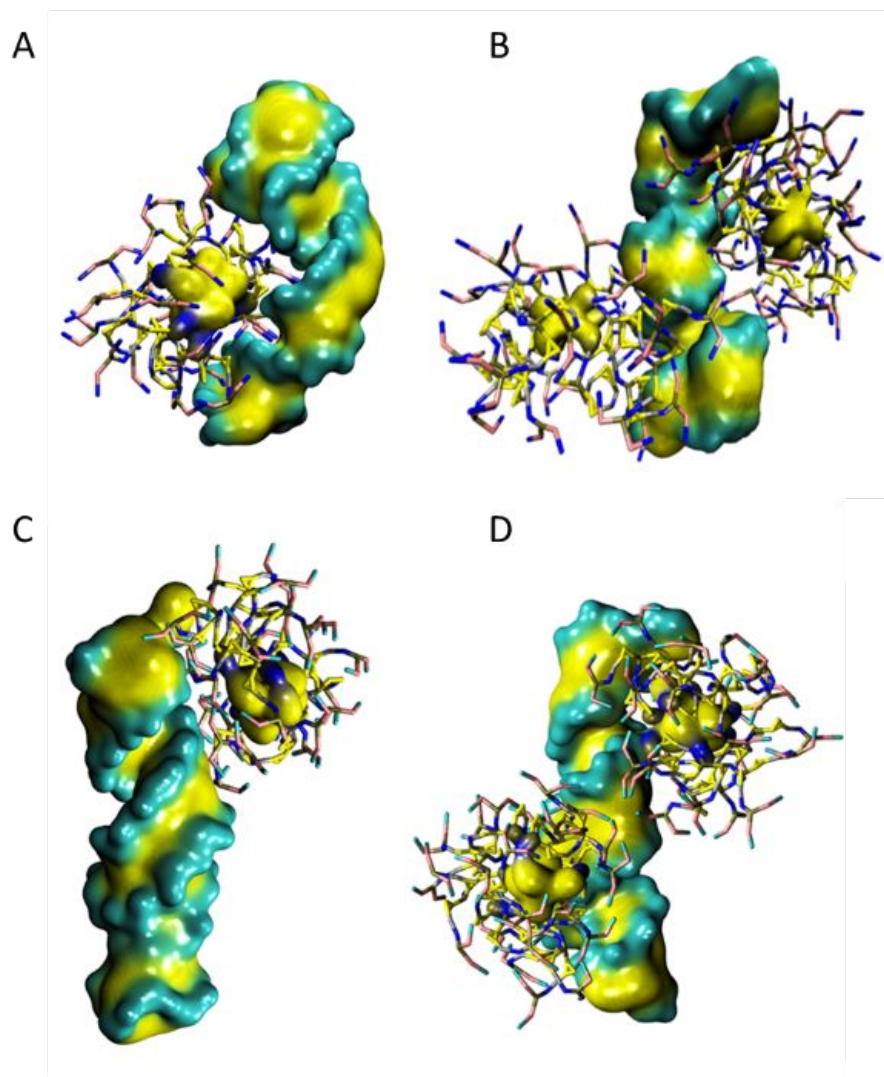
Figure S10: Qualitatively representation of dendrimers-siRNA complexation behavior. In picture (A) 1 DM in complexation with siRNA is shown (40.1% of MD frames), while in picture (B) 2 DM in complexation with siRNA are represented (59.9% of MD frames). In picture (C) 1 DP in complexation with siRNA is shown (20.2% of MD frames), while in picture (D) 2 DP in complexation with siRNA are represented (79.8% of MD frames).

References

(1)   Curtis, D. E.; Vandermeersch, T.; Hutchison, G. R.; Lonie, D. C.; Zurek, E.; Hanwell, M. D. Avogadro: An Advanced Semantic Chemical Editor, Visualization, and Analysis Platform. *J. Cheminform.* **2012**, *4* (1), 17. https://doi.org/10.1186/1758-2946-4-17.

(2)   Dupradeau, F. Y.; Pigache, A.; Zaffran, T.; Savineau, C.; Lelong, R.; Grivel, N.; Lelong, D.; Rosanski, W.; Cieplak, P. The R.E.D. Tools: Advances in RESP and ESP Charge Derivation and Force Field Library Building. *Phys. Chem. Chem. Phys.* **2010**, *12* (28), 7821–7839. https://doi.org/10.1039/c0cp00111b.

(3)   Schmidt, M. W.; Baldridge, K. K.; Boatz, J. A.; Elbert, S. T.; Gordon, M. S.; Jensen, J. H.; Koseki, S.; Matsunaga, N.; Nguyen, K. A.; Su, S.; General Atomic and Molecular Electronic Structure System. *J. Comput. Chem.* **1993**, *14* (11), 1347–1363. https://doi.org/10.1002/jcc.540141112.

(4)   Wang, J.; Wolf, R. M.; Caldwell, J. W.; Kollman, P. A.; Case, D. A. Development and Testing of a General Amber Force Field. *J. Comput. Chem.* **2004**, *25* (9), 1157–1174. https://doi.org/10.1002/jcc.20035.

(5)   Kutzner, C.; Páll, S.; Fechner, M.; Esztermann, A.; Groot, B. L.; Grubmüller, H. More Bang for Your Buck: Improved Use of GPU Nodes for GROMACS 2018. *J. Comput. Chem.* **2019**, *40* (27), 2418–2431. https://doi.org/10.1002/jcc.26011.

(6)   Abraham, M. J.; Murtola, T.; Schulz, R.; Páll, S.; Smith, J. C.; Hess, B.; Lindah, E. Gromacs: High Performance Molecular Simulations through Multi-Level Parallelism from Laptops to Supercomputers. *SoftwareX* **2015**, *1–2*, 19–25. https://doi.org/10.1016/j.softx.2015.06.001.

(7)   Bussi, G.; Donadio, D.; Parrinello, M. Canonical Sampling through Velocity Rescaling. *J. Chem. Phys.* **2007**, *126* (1). https://doi.org/10.1063/1.2408420.

(8)   Berendsen, H. J. C.; Postma, J. P. M.; Van Gunsteren, W. F.; Dinola, A.; Haak, J. R. Molecular Dynamics with Coupling to an External Bath. *J. Chem. Phys.* **1984**, *81* (8), 3684–3690. https://doi.org/10.1063/1.448118.

(9)   Parrinello, M.; Rahman, A. Polymorphic Transitions in Single Crystals: A New Molecular Dynamics Method. *J. Appl. Phys.* **1981**, *52* (12), 7182–7190. https://doi.org/10.1063/1.328693.

(10)   Essmann, U.; Perera, L.; Berkowitz, M. L.; Darden, T.; Lee, H.; Pedersen, L. G. A Smooth Particle Mesh Ewald Method. *J. Chem. Phys.* **1995**, *103* (19), 8577–8593. https://doi.org/10.1063/1.470117.

(11)   Johnson, J. K.; Zollweg, J. A.; Gubbins, K. E. The Lennard-Jones Equation of State Revisited. *Mol. Phys.* **1993**, *78* (3), 591–618. https://doi.org/10.1080/00268979300100411.

(12)   Marrink, S. J.; Risselada, H. J.; Yefimov, S.; Tieleman, D. P.; Vries, A. H. De. The MARTINI Force Field : Coarse Grained Model for Biomolecular Simulations The MARTINI Force Field : Coarse Grained Model for Biomolecular Simulations. *J. Phys. Chem. B* **2007**, *111* (June), 7812–7824. https://doi.org/10.1021/jp071097f.

(13) Mantha, S.; Yethiraj, A. Conformational Properties of Sodium Polystyrenesulfonate in Water: Insights from a Coarse-Grained Model with Explicit Solvent. *J. Phys. Chem. B* **2015**, *119* (34), 11010–11018. https://doi.org/10.1021/acs.jpcb.5b01700.

(14) Riniker, S.; Allison, J. R.; Van Gunsteren, W. F. On Developing Coarse-Grained Models for Biomolecular Simulation: A Review. *Physical Chemistry Chemical Physics*. The Royal Society of Chemistry August 22, 2012, pp 12423–12430. https://doi.org/10.1039/c2cp40934h.

(15) Moore, T. C.; Iacovella, C. R.; Mccabe, C. Derivation of Coarse-Grained Potentials via Multistate Iterative Boltzmann Inversion The Multiscale Coarse-Graining Method. I. A Rigorous Bridge between Atomistic and Coarse-Grained Models On the Representability Problem and the Physical Meaning of Coarse. *Cit. J. Chem. Phys.* **2014**, *140* (22), 44108. https://doi.org/10.1063/1.4880555.

(16) Reith, D.; Pütz, M.; Müller-Plathe, F. Deriving Effective Mesoscale Potentials from Atomistic Simulations. *J. Comput. Chem.* **2003**, *24* (13), 1624–1636. https://doi.org/10.1002/jcc.10307.

(17) Banerjee, P.; Roy, S.; Nair, N. Coarse-Grained Molecular Dynamics Force-Field for Polyacrylamide in Infinite Dilution Derived from Iterative Boltzmann Inversion and MARTINI Force-Field. *J. Phys. Chem. B* **2018**, *122* (4), 1516–1524. https://doi.org/10.1021/acs.jpcb.7b09019.

(18) Milano, G.; Goudeau, S.; Müller-Plathe, F. Multicentered Gaussian-Based Potentials for Coarse-Grained Polymer Simulations: Linking Atomistic and Mesoscopic Scales. *J. Polym. Sci. Part B Polym. Phys.* **2005**, *43* (8), 871–885. https://doi.org/10.1002/polb.20380.

(19) Kremer, K.; Bürger, T.; Batoulis, J.; Hahn, O.; Tschöp, W. Simulation of Polymer Melts. I. Coarse-Graining Procedure for Polycarbonates. *Acta Polym.* **2002**, *49* (2–3), 61–74. https://doi.org/10.1002/(sici)1521-4044(199802)49:2/3<61::aid-apol61>3.0.co;2-v.

(20) Graham, J. A.; Essex, J. W.; Khalid, S. PyCGTOOL: Automated Generation of Coarse-Grained Molecular Dynamics Models from Atomistic Trajectories. *J. Chem. Inf. Model.* **2017**, *57* (4), 650–656. https://doi.org/10.1021/acs.jcim.7b00096.

(21) Uusitalo, J. J.; Ingólfsson, H. I.; Marrink, S. J.; Faustino, I. Martini Coarse-Grained Force Field: Extension to RNA. *Biophys. J.* **2017**, *113* (2), 246–256. https://doi.org/10.1016/j.bpj.2017.05.043.

(22)   Ramírez, C. L.; Petruk, A.; Bringas, M.; Estrin, D. A.; Roitberg, A. E.; Marti, M. A.; Capece, L. Coarse-Grained Simulations of Heme Proteins: Validation and Study of Large Conformational Transitions. *J. Chem. Theory Comput.* **2016**, *12* (7), 3390–3397. https://doi.org/10.1021/acs.jctc.6b00278.

(23)   Marrink, S. J.; Tieleman, D. P. Perspective on the Martini Model. *Chem. Soc. Rev.* **2013**, *42* (16), 6801. https://doi.org/10.1039/c3cs60093a.

(24)   Monticelli, L.; Bulacu, M.; Goga, N.; Periole, X.; Rossi, G.; Marrink, S. J.; Tieleman, D. P.; Zhao, W. Improved Angle Potentials for Coarse-Grained Molecular Dynamics Simulations. *J. Chem. Theory Comput.* **2013**, *9* (8), 3282–3292. https://doi.org/10.1021/ct400219n.